Influence of equal-channel angular pressing on the microstructure and corrosion behaviour of a 6xxx aluminium alloy for automotive conductors

Clement Rochet, M. Veron, E.F. Rauch, T.C. Lowe, B. Arfaei, A. Laurino, J.P. Harouard, Christine Blanc

Clement Rochet, M. Veron, E.F. Rauch, T.C. Lowe, B. Arfaei, et al.. Influence of equal-channel angular pressing on the microstructure and corrosion behaviour of a 6xxx aluminium alloy for automotive conductors. Corrosion Science, 2020, 166, pp.108453. ⟨10.1016/j.corsci.2020.108453⟩. ⟨hal-03082058⟩

HAL Id: hal-03082058
https://hal.science/hal-03082058v1

Submitted on 7 Mar 2022

Influence of Equal-Channel Angular Pressing on the Microstructure and Corrosion Behaviour of a 6xxx Aluminium Alloy for Automotive Conductors

C. Rochet[1,2], M. Veron[3], E.F. Rauch[3], T.C. Lowe[4], B. Arfaei[5], A. Laurino[2], J.-P. Harouard[2], C. Blanc[1,*]

[1] CIRIMAT, Université de Toulouse, CNRS, INPT-ENSIACET, 4 allée Emile Monso, CS 44362, 31030 Toulouse cedex 04, France
[2]LEONI WIRING SYSTEMS FRANCE, 5 Avenue de Newton, 78180 Montigny-le-Bretonneux, France
[3]Université Grenoble Alpes, CNRS, Grenoble INP, SIMAP, 38000 Grenoble, France
[4]Colorado School of Mines, Dept. of Metallurgical and Materials Engineering, Golden, CO 80401, USA
[5]Ford Motor Company, Research and Advanced Engineering, Palo Alto, CA 95134, USA

*Corresponding author. Tel/fax: +33 (0)5 34 32 34 07/+33 (0)5 34 32 34 98

E-mail address: christine.blanc@ensiacet.fr

Present address: CIRIMAT, Université de Toulouse, CNRS, INP-ENSIACET, 4 allée Emile Monso - BP 44362, 31030 Toulouse cedex 4, France

Abstract

An Al-Mg-Si aluminium alloy was shaped by using a two-pass equal-channel angular pressing (ECAP) process. This led to fragmentation of the coarse Fe-rich intermetallics (IMCs), a decrease in grain size and an increase in the high angle grain boundary (HAGB) density, with overconcentration of HAGBs around the IMCs. Corrosion tests in NaCl solution showed that, before and after ECAP, only pitting corrosion occurred. However, for ECAP samples, pits were more numerous due to the fragmentation of the IMCs; they were also larger and less deep, their propagation being strongly influenced by the presence of very small grains around the IMCs.

Keywords

A. Aluminium; A. Intermetallics; B. SEM; B. TEM; C. Pitting Corrosion; C. Interfaces

1 Introduction

The automotive industry is facing increasing ecological and economical challenges. Reducing greenhouse gas emissions and fossil fuel dependence has become a priority for car manufacturers. In this context, new materials are to be used in order to reduce both weight and cost of automotive components. Wires are currently made of copper and represent almost 50 kg of the full vehicles mass. The replacement of copper with aluminium alloys could enable car manufacturers to reduce the cost and the specific mass of the wires by 50%.

However, the use of aluminium alloys for wires leads to new technological constraints emerging from the complexity of the automotive environment. Indeed, the combination of aggressive media (de-icing road salt, coolant, and windshield washer fluid), varying temperatures and vibrations induces different types of wiring harness corrosion damage.

For these reasons, automotive wires require a combination of high mechanical strength, high conductivity and high corrosion resistance. Al-Mg-Si alloys match these requirements and are already used for automotive wiring applications [1,2]. The conventional forming process of aluminium wires consists in alternated steps of deformation (drawing) and thermal treatments. Unfortunately, aluminium alloys are less conductive than copper, and aluminium wires require larger sections to carry the same amperage as copper wires. Severe plastic deformation (SPD) is a potential route to bypass these limitations.

Indeed, SPD processes were developed years ago as a viable way to improve mechanical and forming properties of metallic alloys through grain refinement [3]. Among those, Equal-Channel Angular pressing (ECAP) is now a very common process to obtain Ultra-Fine Grain (UFG) microstructures with highly enhanced mechanical properties [4–10]. ECAP consists of pressing a bar through a die with a given angle. It applies high strain by shear deformation without any change in cross-section of the material [11]. Many studies focus on the influence of SPD (and ECAP) on the microstructure of aluminium alloys (AA), e.g. Al-Mg-Si alloys

[4,12–14]. Khelfa et al. observed a 97% decrease in the grain size after only one ECAP pass in AA 6060 T6 [15]. Sitdikov et al. showed the evolution of the texture during ECAP processing in Al-Mg-Sc alloy [16]. It is now clear that SPD strongly modifies basic microstructural parameters such as grain size and morphology, texture and the nature of boundaries. Furthermore, intermetallic coarse particles (IMCs) can also be affected by SPD processes shown to be effective in reducing, by fragmentation, the IMC size [17]. Finally, another interesting feature of ECAP is the possibility to combine high strain and heat treatments to enhance precipitation kinetics in order to maximise mechanical and electrical properties of Al-Mg-Si alloys. For example, Murashkin et al. managed to obtain ß' hardening precipitates during ECAP at 130°C in AA 6101 [4]. They noticed an increase in both mechanical strength and electrical conductivity of the samples compared to conventional thermo-mechanical treatments of Al-Mg-Si alloys.

These microstructural changes could have a strong influence on the corrosion behaviour of aluminium alloys processed by SPD, and by ECAP in particular. Indeed, it is well known that the corrosion behaviour of aluminium alloys is strongly related to the precipitates present in the material. The role of intergranular ß-Mg_2Si precipitates possibly formed during aging of Al-Mg-Si alloys has been studied in the literature [18–23]. These precipitates are associated with intergranular corrosion, due to their differences in reactivity as compared to the surrounding matrix and/or the precipitate free zone. However, many studies have also shown that Fe-rich intermetallic coarse (IMC) particles formed during the alloy solidification play a key role in the corrosion mechanisms of Fe-containing aluminium alloys by acting as cathodes with respect to the surrounding matrix and therefore as pit initiation sites [23–25]. Considering now the influence of ECAP on the corrosion behaviour, different studies have shown an increase in the corrosion rate after ECAP associated with the activity of intermetallic particles affected by shear deformation [12,26]. The severity of corrosion for samples after SPD processes could be related to the multiplication of pit initiation sites only due to IMC fragmentation, suggesting an influence of ECAP on pit initiation. But, it could be also explained by considering more complicated effects, e.g. local deformation of the matrix around the IMCs. Furthermore, many studies have also shown a relationship between grain size and corrosion behaviour; Ralston et al. proposed a review of the pertinent literature combined with their own work to analyse this relationship [27]. They showed that two cases have to be considered to understand the effect of the grain size on the corrosion rate: the first one corresponds to materials that exhibit active corrosion, whereas the second case corresponds to materials with low to passive-dissolution rates. Such a differentiation should help explain the controversy that exists when dealing with the influence of ECAP on the corrosion behaviour of aluminium alloys, ECAP being found to both increase and decrease the corrosion rate [12,26–31]. Moreover, the complexity of establishing a relationship between the corrosion behaviour and the grain size could also be explained by considering the diversity of the interfaces, i.e. their level of misorientation. For example, the susceptibility to intergranular corrosion of aluminium in HCl was found to be strongly related to the grain boundary misorientation distribution [32]. In any event, these features of the microstructure are to be linked to the corrosion propagation, suggesting that ECAP should influence the corrosion in-depth propagation.

Therefore, it remains of great interest to evaluate the extent to which ECAP can improve mechanical and electrical properties of Al-Mg-Si alloys without decreasing their corrosion resistance. Therefore, the present study aims to analyse the influence of two ECAP-based forming processes on the microstructure and the corrosion behaviour of an Al-Mg-Si aluminium alloy. To do so, the critical microstructural parameters modified by ECAP were studied. Close attention was paid to the size and distribution of IMCs along with the presence of β-Mg_2Si type intragranular and intergranular precipitates before and after ECAP. The grains structure, the texture and the nature of boundaries were also considered as key parameters in this study. Such an approach was enabled by performing scanning and transmission electron microscopy and electron backscatter diffraction. The relationship between these microstructural changes and the corrosion susceptibility of the alloy was then investigated by analysing the corrosion damage for samples before and after ECAP process. Corrosion tests were performed in an aggressive medium, i.e. a chloride-containing environment, and under polarisation for a fixed current density, so that corrosion propagation was the main focus of this study, although corrosion initiation was also important.

2 Material and methods

2.1 Materials

The material studied was an Al-Mg-Si aluminium alloy provided as extruded rods (9.5 mm in diameter) with the following chemical composition (wt. %, Al balance): Mg 0.57, Si 0.37, Fe 0.10, Mn 0.04, Cu 0.01, others 0.10. The as-received condition was considered as the reference state in the following.

The as-received samples underwent two different ECAP processes referred as ECAP-RR and ECAP-RH. ECAP was performed using an ECAP-Conform machine with a 120° die angle [33].

1. ECAP-RR consisted of two passes at room temperature with a displacement rate of 2.04 mm/s ($\varepsilon = 1.14$) and a rotation of 90° between passes [34].
2. ECAP-RH consisted of one pass at room temperature and one pass at 135-155°C with the same displacement rate for both passes of 2.04 mm/s ($\varepsilon = 1.14$) and a rotation of 90° between passes.

Two types of samples were studied: transverse and longitudinal sections referred as TS and LS. All samples were ground with SiC abrasive paper 1200 and 2400 and then polished with diamond paste down to ¼ µm. Several steps of ultrasonic cleaning using demineralised water were added. As said in the introduction, it should be pointed out here that the influence of ECAP on the corrosion behaviour of the alloy is studied in this work considering the corrosion propagation that occurs in the body of a rod. The presence of an altered surface layer, linked to the forming process or the polishing step during sample preparation, could modify the corrosion initiation through the surface developed on a wire strand, but this is not the focus of this study.

2.2 Experimental methods and techniques

2.2.1 Analysis of the microstructure

An optical microscope (OM, MA200 Nikon) was used to characterise the global distribution and morphology of IMCs. Before observations, samples were ground using SiC abrasive paper down to 2400, then polished with diamond paste down to 0.25 µm and finally using colloidal silica (OPS) for 30 s. A Scanning Electron Microscope (SEM, Quanta 450 by FEI) combined with Energy Dispersive X-ray Spectroscopy (EDS Bruker) was also used in order to determine the chemical composition, the surface density and the size distribution of IMCs. For the surface area covered by the IMCs, an image processing using ImageJ software was applied on SEM images obtained using backscattered electrons. For each sample, a cumulated average of the fraction of surface area was calculated each time a new image was post-processed until a stabilisation of the average was observed, which was obtained after the analyses of about 25-30 images, depending on the sample. Analysis of the crystallographic structure of the dispersoids and IMCs was performed using Transmission Electron Microscopy (TEM) with a Field-Emission Gun operating at 200 kV (FEG-TEM, JEOL JEM 2100 F, Raimond Castaing Microanalysis Center, Toulouse, France). TEM was also useful to analyse the nature and distribution of fine intragranular and intergranular precipitates. For these last observations, samples were ground with SiC abrasive paper 1200, 2400 and 4000 down to 80 µm, cut in discs of 3 mm diameter and electropolished at -15°C in TenuPol-5 with 900 mL of CH_3OH and 300 mL of HNO_3.

Electron Back-Scatter Diffraction (EBSD) analyses were also performed for all samples in order to determine the grain size, the global texture and the nature of boundaries. For this analysis, samples were prepared as detailed above with the addition of a 90 s polishing step with colloidal silica. EBSD patterns were collected using an Oxford Instruments HKL EBSD System (Nordlys NanoEBSD detector) and then analysed using ATEX software [35]. The EBSD detector was mounted on a JEOL JSM 7100F SEM with a Field-Emission Gun operating at 20 kV. EBSD data were also post-processed using the commercial software package Oxford Channel 5. Post-processing was performed according to ASTM Standard E2627. Large fields of view of 450 x 600 µm were studied using a 0.5 µm step to characterise the global texture of the samples. Small fields of view of 120 x 90 µm were also analysed with a 0.07 µm step size in order to obtain more accurate data for grain size and interface densities. Grains boundaries and sub-grain boundaries were defined as a local interface possessing a misorientation larger than 2°. High Angle Grain Boundaries (HAGBs) and Low Angle Grain Boundaries (LAGBs) were distinguished as having a misorientation larger than 10°, or between 2 and 10°, respectively. Only grains larger than 200 nm were taken into account.

Finally, an analysis of the grain structure and the local deformations surrounding IMCs was performed for all samples using Automated Crystallographic Orientation Mapping (ACOM) in SiMaP (Grenoble) [36]. The analysis was performed in a Transmission Electron Microscope with a Field-Emission Gun operating at 200 kV (FEG-TEM, JEOL JEM 2100 F). Each map was acquired using a 20 nm step size and a precession angle of 1.2°. The samples used were identical to those which were used for TEM analysis. As for EBSD analysis, a 10° misorientation criteria was used to classify the boundaries, i.e. HAGBs and LAGBs.

2.2.2 Mechanical testing

To better understand the influence of ECAP on the microstructure of the alloy, micro-hardness measurements were performed using a Vickers micro-hardness indenter (Omnimet 2100 by BUEHLER) with a 100 g load. ISO Standard 6507 was followed to perform these tests. Measurements were performed side to side for each sample. The gap g between each indent was chosen in agreement with the following criteria ($g > 2.5d$) where d was the diameter of an indent (around 70 µm). Furthermore, tensile tests were performed using an MTS testing machine equipped with a 5 kN load cell. Cylindrical tensile samples, with a gauge length of 24 mm and a 4 mm diameter, were used. Tests were all performed at a constant strain rate of 10^{-3} s^{-1} using a 20 mm extensometer in order to record sample deformation during testing. For reproducibility, at least three tensile samples were tested for each condition.

2.2.3 Characterisation of the corrosion behaviour

The corrosion behaviour of the alloy was first studied by plotting polarisation curves using a three-electrode cell with a platinum and a saturated calomel electrode acting as counter and reference electrodes, respectively. All electrochemical measurements were performed by using a VSP-128 Biologic Potentiostat. Chloride-containing solutions are the reference electrolyte used for industrial tests; they are the most representative of the automotive environment, e.g. de-icing salts. Clearly, other pollutants can be found but it was not the aim of this paper to study the influence of these chemical species. Therefore, all corrosion experiments were performed in a quite aggressive electrolyte, i.e. a 0.5 M NaCl solution. Potentiodynamic polarisation curves were plotted after 60 minutes at the open-circuit potential (OCP) in NaCl solution. Cathodic and anodic parts were acquired separately, from OCP + 5 mV and OCP - 5 mV for cathodic and anodic parts, respectively. The potential sweep rate was 250 mV h^{-1}. Each measurement described below was reproduced at least 5 times to ensure the reproducibility of results.

Then, the corrosion morphology obtained after the polarisation tests was analysed using OM (MA200 Nikon) and SEM (Quanta 450 by FEI). An accurate analysis of the pit propagation was also performed by using a confocal microscope (Sensofar S Neox): in that case, samples were maintained at OCP for 5 min and then polarised under a fixed current density (100 µA cm^{-2}, 1 mA cm^{-2} and 7 mA cm^{-2}) for 10 min in order to compare the corrosion propagation for a similar charge passed for the different microstructures. It could be noted here that those tests under polarisation could be considered as representative of the in-service conditions considering the current flow seen by the cables. The pit density, average pit depth and the corroded surface ratio were determined using a confocal microscope along with Gwyddion analysis software. A quantitative analysis was performed on two different samples for each condition. Approximately 900 pits were analysed for each condition.

In the end, in order to investigate the influence of local deformation of the matrix surrounding IMCs in corrosion propagation mechanisms, a Transmission Kikuchi Diffraction (TKD) analysis was performed for the longitudinal section of the as-received condition only. The samples were TEM slices obtained with the preparation method used for TEM analysis. TKD analysis consisted in the acquisition of small scale orientation maps (12 µm x 6 µm) with a step size of 40 nm. Observations of a selected zone were performed before immersion, after a 12-hour immersion in 3 M NaCl and after a 24-hour immersion in 3 M NaCl. Post-processing of the images was performed using the same method as described in 2.2.1.

3 Results and discussion

3.1 Influence of ECAP on the microstructure of the Al-Mg-Si Alloy

3.1.1 Grain morphology and nature of the boundaries

The orientation maps obtained for the transverse and longitudinal sections of as-received, ECAP-RR and ECAP-RH samples are given in Fig. 1. In these maps, the colour code refers to the crystallographic orientation of each grain along the extrusion direction (Z and X for the transverse and the longitudinal sections, respectively). Firstly, for all samples, grains were strongly elongated along the forming direction, due to the extrusion process, with the formation and arrangement of dislocations into dislocation walls aligned along the forming direction, i.e. in the longitudinal section [37–38]. This may introduce difficulties in analysing the grain structure. Thus, only transverse sections will be discussed in the following. Fig. 1 shows that grain refinement occurred during ECAP-RR and ECAP-RH processes. Based on observations of the orientation maps (Figs. 1d, e, g and h), the grain size was smaller for ECAP-RR compared to ECAP-RH. Additionally, Fig. 2a shows that the proportion of grains (calculated considering the number of grains) with an average diameter under 1 µm was increased by 31 % and 17 % for ECAP-RR and ECAP-RH, respectively, compared to the as received sample. On the contrary, the proportion of grains with an average diameter comprised between 5 and 10 µm was decreased by 85 % and 80 % for ECAP-RR and ECAP-RH samples, respectively. Overall, these first observations suggested a more efficient refining process during ECAP-RR when compared to ECAP-RH. However, both as-received and ECAP-RR samples showed a heterogeneous grain structure in comparison with ECAP-RH samples, for which more than 50% of the surface was occupied by grains ranging from 1 to 5 µm in diameter (Fig. 2b). The complexity of the microstructures was clearly seen in Figs. 1f and i that correspond to band contrast images with identification of the grain boundaries for ECAR-RR and ECAP-RH samples, respectively. For ECAP-RR sample, small grains were observed, but also some larger grains, whereas, for ECAP-RH sample, the microstructure was more homogeneous with large surface areas covered by very small grains. Therefore, it appeared that the determination of the grain size for such heterogeneous structures could not be limited to the calculation of average grain size taking into account the number of grains with a given diameter. The surface occupied by large and small grains had to be taken into account in order to give an accurate estimation of the average grain size. Following this method, area weighted average grain size was calculated for all the samples; it decreased from 24 µm for the as-received sample to 16 µm for the ECAP-RR sample and finally 4 µm for the ECAP-RH sample, which showed a higher refinement efficiency for the ECAP-RH process. Assuming that these last values were the relevant ones, the alternative conclusions about grain size based on qualitative interpretation of Fig. 1d, e, g and h could be explained by the colour code used to identify crystallographic orientations and not grain boundaries. Comparison of our results to the literature highlighted the importance of the methodology used to calculate the average grain size. Indeed, in agreement with our results, many studies showed a grain refinement during SPD that resulted from both dynamic recovery and continuous dynamic recrystallisation (CDRX) [39–42]. CDRX generally happened during high temperature deformation; during low temperature ECAP, grain refinement was only attributed to the subdivision of coarser grains and the distortion of smaller ones [43–44]. Previous reports have shown that a higher processing temperature leads to larger grains when compared to low temperature deformation [45–49]. For example, Goloborodko et al. processed samples up to strains of 12% at temperatures ranging from 250 °C to 400 °C and showed an increase in the grain size associated with increasing processing temperature [47]. The apparent discrepancy with our results could be explained considering first the methodology used to calculate the average grain size. Moreover, it should also be pointed out that both strain and temperature used in Goloborodko’s work were higher than those used in our ECAP processes; therefore, the recrystallisation process could have been combined with a coarsening of the recrystallised grains for the highest temperatures. More generally, it should be noticed that, in the present study, the effect of ECAP on the grain size was very low when compared to the results of the literature [4]. This might be due to the initially fine grain structure of the as-received sample.

Fig. 3a shows the relative fraction of HAGBs and LAGBs for each sample. Due to the high elongation of grains in the longitudinal section, it was difficult to determine the density of boundaries for these sections. Therefore, only results for the transverse sections are discussed. Results showed that the relative fraction of HAGBs was increased by 80% and 147% for ECAP-RR and ECAP-RH samples, respectively. Those results were consistent with previous conclusions, i.e. a decrease in the grain size with ECAP and a smaller average grain size for ECAP-RH samples. Indeed, as stated in the literature, grain refinement during ECAP was commonly linked to the formation of HAGBs due to recrystallisation processes [15,28,45]. To confirm these results and avoid the problems due to the identification of grains, the total length of boundaries was calculated for each sample (Fig. 3b). An increase in the total length of boundaries was observed after ECAP, in particular after ECAP-RH. Furthermore, for ECAP-RR and ECAP-RH samples, the length of both HABGs and LAGBs increased compared to the as-received sample, with a very strong increase in the total length of HAGBs for ECAP-RH sample. Those results clearly showed that the increase of processing temperature during ECAP-RH enabled a homogeneous recrystallisation phenomenon leading to small recrystallised grains; the temperature was not high enough to lead to a coarsening of the recrystallised grains. After ECAP-RR, because of the lower temperature during the deformation process, a more heterogeneous microstructure was obtained due to an incomplete recrystallisation process; it combined large and small grains, the smallest ones being formed either by a recrystallisation process or by the subdivision of larger grains during deformation.

3.1.2 Texture Analysis

Pole figures obtained for the transverse and longitudinal planes of the as-received ECAP-RR and ECAP-RH samples are shown in Fig. 4. These demonstrate, in agreement with Fig. 1, a strong effect of ECAP processes on the global texture of the alloy. The as-received sample exhibited two fiber texture components parallel to the extrusion axis, which are typical for this type of forming process [50–52]. The major component was the <111> direction and the minor one was the <100> direction, which is the typical case for high stacking fault energy fcc materials such as aluminium [53–54]. After ECAP-RR, a strong change in the texture was observed, characterised by a randomisation of the texture of the alloy highlighted by a "blurring" of the pole figures and a decrease in the maximum texture intensity from 15 times-random for the as-received sample to 4 times-random for the ECAP-RR sample. On the contrary, the ECAP-RH sample exhibited a texture which was quite similar to the as-received sample. Besides, the maximum texture intensity was higher for the ECAP-RH sample than for the ECAP-RR sample. Texture development during ECAP is strongly dependent on the processing parameters such as the die angle and the number of passes. Therefore, it becomes very difficult to predict and interpret the changes in texture after several passes [55]. However, some authors have observed a texture weakening after the first passes of deformation [14,55–56]. Ciemiorek et al. noticed a texture randomisation during incremental ECAP for an aluminium alloy [14]. According to this study, this was related to the activation of shearing planes and the rotation of grains due to high deformation. In the present study, the major direction for the ECAP-RR sample was <110>, which is typical for a simple shear [14,16,57]. The texture observed for the ECAP-RH sample could be explained considering a more efficient CDRX process in the final stage of deformation, which resulted in grain orientations closer to what we can expect from the extrusion process. This was consistent with the conclusions drawn from the grain structure analysis. Furthermore, the heterogeneity of the texture distribution for ECAP-RR sample could contribute to explain the deceptive appearance of small grain size (Fig. 1d) discussed above. To conclude here, the results showed that the second pass in the ECAP process had a major influence on texture modifications, and more globally on microstructural changes.

3.1.3 Influence of ECAP on the precipitation states

Firstly, attention was paid to the influence of ECAP on the distribution and size of IMCs, considering, as explained in the introduction, that IMCs are preferential pit initiation sites for Al-Mg-Si alloys. OM and SEM observations showed IMCs of different sizes in all samples: they were aligned along the extrusion axis due to the forming process of the rods (Fig. 5a and 5b) [24]. Most of them were identified as Fe-rich IMCs using EDS analyses. Additional observations by TEM (Fig. 6a) allowed typical IMCs to be observed; EDX analyses confirmed that most of the IMCs contained Al, Fe, Mg and Si in various amounts. Moreover, the diffraction pattern of an Al-Fe-Si IMC, shown in Fig. 6a, corresponded to the $Al_9Fe_2Si_2$ compound characterised by an orthorhombic crystal structure (a = b = 0.615 nm, c = 2.08 nm) [24]. It should be pointed out that many other phases have been identified in the literature in 6xxx aluminium alloys [2,58–59]. In the present work, whereas most of the IMCs were identified as $Al_9Fe_2Si_2$ compounds, some very rare IMCs were found to be of the Al-Mg-Si type, which have already been observed in the literature for this type of alloy [60]. However, attention was paid to Fe-rich IMCs only. Observations showed that the structure and the global morphology of IMCs were identical after ECAP-RR and ECAP-RH. The fraction of surface area covered by Fe-rich IMCs was then calculated; for each sample, a similar image processing was performed by considering different values of the threshold fixed to identify a Fe-rich IMC. Three sets of analyses were performed: the fraction of surface area covered by Fe-rich IMCs was therefore calculated by considering only IMCs with a minimum surface area of 0.001 μm², 0.005 μm², and 0.01 μm². Results showed that there were not significant differences between the different sets of analyses, and that a threshold equal to 0.01 μm² was a good compromise. Fig. 5c shows a decrease in the surface area covered by IMCs after ECAP-RR and ECAP-RH. Additionally, Fig. 5d shows that the distribution of the IMCs size was affected by ECAP, in particular for the ECAP-RH process, which led to a higher proportion of small IMCs. This result could be explained by considering the breakdown of IMCs during ECAP. This has already been reported in the literature and explained by the high shearing stress applied to IMCs during ECAP [12,61]. Clearly, the decrease in size of the IMCs could also explain the decrease in the fraction of surface area covered by the IMCs (Fig. 5c), the smallest IMCs being not taken into account in the calculation. Results also showed that the same surface area covered by the IMCs was measured for both ECAP-RR and RH samples (Fig. 5c), whereas only the size distribution plotted for the ECAP-RH sample was modified compared to the as-received sample.

Accordingly, the results described above showed that the ECAP processes had an influence on the size and distribution of IMCs which could modify the pitting corrosion behaviour of the alloy by multiplying the potential pit initiation sites. However, it is also true that β-Mg_2Si type intergranular and intragranular (hardening) precipitates can play a key role concerning the corrosion behaviour of Al-Mg-Si alloys. Thus, TEM observations were then focused on these types of precipitates. Those observations did not reveal any intragranular or intergranular precipitation (Fig. 6b). This result seemed relevant for the as-received and ECAP-RR samples, whereas those precipitates could have been expected for the ECAP-RH sample for which the deformation at 150°C was expected to lead to the formation of β''/β' strengthening precipitates. Two hypotheses could thus be proposed:

- The as-received sample was not in a solution-treated state. This was strongly suggested by the fine and highly deformed microstructure observed. It is well known that static or dynamic precipitation hardening is linked to the supersaturation in alloying elements and high vacancy concentration resulting from quenching of the solution heat treated state, those vacancies serving as nucleation sites for GP zones [62]. In the present work, it was very unlikely that the as-received sample was supersaturated preventing any precipitation hardening (static or dynamic).
- Another reason could be that the ECAP-RH conditions did not promote precipitation strengthening. Indeed, Hirosawa et al. showed that the temperature during ECAP is of major importance due to the large amount of dislocations and grain boundaries in highly deformed state which act as heterogeneous nucleation sites for stable phases and reduce the precipitation of strengthening phases. This phenomenon is called competitive precipitation [63]. One could easily assume that such phenomenon could also occur during ECAP-RH. TEM observations showed large dislocation arrays for ECAP samples (Fig. 6c). These features were most likely introduced by the high amount of deformation induced during ECAP [5,9,12,38].

3.2 Influence of ECAP on the mechanical properties of the Al-Mg-Si alloy

For all samples, results of Vickers micro-hardness measurements were quite similar in both transverse and longitudinal sections. For the as-received sample, the average micro-hardness value was around 62 ± 3 HV, which was consistent with previous studies on aluminium alloys with similar forming conditions [2,64]. After the ECAP-RR and ECAP-RH processes, the average micro-hardness was increased to 85 ± 3 HV and 78 ± 3 HV, respectively, highlighting the strengthening effect of ECAP. According to Hall-Petch's Law, higher micro-hardness values could be expected for the ECAP-RH sample, considering the fraction of surface area covered with small grains (Fig. 2) [13,65]. However, some authors have criticised the validity of Hall-Petch's Law for ultra-fine grained microstructures [66–67]. In addition, a higher density of LAGBs was measured for the ECAP-RR sample (Fig. 3a), which could indicate a higher amount of stored deformation inside grains, in agreement with previous conclusions concerning the incomplete recrystallisation process for the ECAP-RR sample compared to the ECAP-RH sample [45]. Therefore, the increase in processing temperature for ECAP-RH, leading to a complete recrystallisation process, would induce a decrease in the deformation stored in grains (dislocations), and consequently a slight softening of the alloy. This particular effect of high temperature processing during SPD has already been observed in other studies [53,68].

The results of tensile tests (Fig. 7) were in good agreement with micro-hardness measurements, showing an increase in $R_{p0.2}$ and R_m along with a decrease in the ductility for both ECAP-RR and ECAP-RH conditions. Moreover, ECAP-RR showed a lower elongation to fracture, and higher $R_{p0.2}$ and R_m values than ECAP-RH in agreement with previous conclusions.

Therefore, results shown in this part showed that ECAP led to a slight improvement of the mechanical properties of the Al-Mg-Si alloy. Corrosion tests were then performed to evaluate the impact of ECAP on the corrosion properties of the alloy.

3.3 Influence of ECAP on the corrosion behaviour of the Al-Mg-Si alloy

3.3.1 Influence of ECAP on the electrochemical response of the Al-Mg-Si alloy

First, polarisation curves were plotted for the as-received, ECAP-RR and ECAP-RH samples after 1 hour at OCP in 0.5 M NaCl; they are reported in Fig. 8. The global shape of the curves was very similar for all samples. Firstly, the cathodic domain (Figs. 8a and c) was characterised by a large current plateau associated with the reduction of dissolved oxygen. Then, the anodic domain (Figs. 8b and d) was characterised by a rapid increase in the current density indicating that the alloy was susceptible to localised corrosion at its corrosion potential. Whatever the section (transverse or longitudinal), E_{corr} values were quite similar for all samples and comprised between -0.72 V/SCE and -0.74 V/SCE. Taking into account that the cathodic process was diffusion controlled, the corrosion current density was considered to be equal to the diffusion-limited current and estimated from the cathodic current densities recorded on the plateau. Values of 2.2 ± 0.2 (1.4 ± 0.7) 10^{-3} mA cm^{-2}, 1.5 ± 0.5 (1.5 ± 0.4) 10^{-3} mA cm^{-2} and 1.5 ± 0.5 (1.6 ± 0.7) 10^{-3} mA cm^{-2} were estimated for the as-received sample, ECAP-RR and ECAP-RH samples, respectively in the transverse (longitudinal) section. Results showed that the standard deviation calculated for each parameter on the basis of at least 5 measurements was quite high when compared to the gap measured between each value. This might be a marker of the strong heterogeneity of the microstructure, in particular for the as-received and ECAP-RR conditions, as pointed out in previous paragraphs. Nevertheless, taking into account these high standard deviations for the corrosion parameters, it was concluded that the polarisation curves did not exhibit a significant influence of ECAP on the corrosion behaviour of the Al-Mg-Si alloy.

OM observations of ECAP-RR sample after polarisation tests in the anodic domain showed that the sample surface was covered with large pits elongated along the forming axis (Fig. 8). This was most likely due to the alignment of IMCs (Fig. 5) and the elongation of grains in this particular direction (Fig. 1). Similar observations were done for both the as-received and ECAP-RH samples. No intergranular corrosion was observed, even for the ECAP-RH sample, which was relevant with the previous TEM observations (Fig. 6) [19,21,69]. Furthermore, OM observations of the samples after immersion at the OCP showed that corrosion pits initiated on the IMCs zone. After only 10 min at the OCP (Fig. 9), SEM observations showed that Fe-rich IMCs acted as cathodes with respect to the matrix, therefore enhancing the preferential dissolution of the latter in NaCl solution. Such a behaviour has been largely reported in the literature and explained referring to differences in composition between IMCs and the surrounding matrix [23–24,70–71]. In that sense, considering only those OM and SEM observations, no modification of the corrosion mechanisms at the OCP and after polarisation in the anodic domain was apparent after ECAP by comparison to the as-received sample, which agreed with the literature [28,72]. Nevertheless, as explained in the introduction, the microstructural features described in part 3.1. were to be linked mostly to the propagation of the corrosion. Therefore, a detailed analysis of the pit propagation was then performed.

3.3.2 Influence of ECAP on the pit propagation in the Al-Mg-Si alloy

To study the pit propagation, samples were polarised in the anodic domain at a fixed current density for 10 min in order to have a similar charge passed for all the samples. Three sets of experiments were performed corresponding to three current density values, i.e. 100 µA cm^{-2}, 1 mA cm^{-2} and 7 mA cm^{-2}, in order to analyse the evolution of the pit morphology when they propagated. A confocal microscope was then used to analyse accurately the morphology of the pits grown. Fig. 10 shows representative 2D profiles obtained by confocal microscopy for the as-received, ECAP-RR and ECAP-RH samples, for both transverse and longitudinal sections, for the three values of current density. First, results clearly showed, as expected, that the higher the current density, the deeper and the larger the pits, whatever the samples. But, the main result concerned the influence of ECAP on the evolution of the pit morphology when the current density increased, i.e. the influence of ECAP on the pit propagation. Indeed, Fig. 10a showed that both the depth and width of the pits were similar for all samples, and whatever the section, for a low current density, i.e. 100 µA cm^{-2}. However, Fig. 10b and c clearly showed that, when the current density increased, i.e. when the pits propagated, a differentiation in the pit morphology was observed depending on the samples and the sections. The pits formed on ECAP samples seemed to gradually become less deep than those formed on the as-received sample, for both transverse and longitudinal sections. Moreover, in the longitudinal section, the pits gradually became larger for ECAP samples as compared to the as-received sample. To complete those experimental results, representative 3D-profiles of pits grown for a current density of 7 mA cm^{-2} were plotted for all samples and both sections (Fig. 11). Comparison of Fig. 11a, c and e for one part, and Fig. 11b, d and f for the other part, clearly showed that pits formed on ECAP samples were less deep, but larger than those formed on the as-received sample. The difference in width was even more marked for the longitudinal section.

Therefore, those first analyses suggested that ECAP strongly impacted the pit propagation. In order to propose a consolidated description of the influence of ECAP on the pit propagation, a statistical analysis was performed: for each condition (i.e., a section and a current density value), two samples were analysed and all the pits observed on those two samples were analysed by confocal microscopy. Then, average values of the pit depth, corroded surface ratio and pit density were calculated (Fig. 12): each average value was calculated from the analysis of about 900 pits. It should be noted here that the pit width was statistically analysed by considering the corroded surface ratio: indeed, surface observations (Fig. 8) clearly showed that the pit did not have a round shape so that it was difficult to define properly the pit width. Therefore, another parameter was considered, i.e. the pit density, which corresponded to the number of pits per cm^2. The combined analysis of those two parameters, i.e. the corroded surface ratio and the pit density, allowed the pit width to be evaluated, and therefore the global lateral propagation of the pit to be described. Fig. 12a confirmed the first hypothesis based on the analysis of representative 2D and 3D profiles: the pit depth was quite similar for all samples for small pits, but, when the pits propagated, pits became less deep for ECAP samples as compared to the as-received sample. Fig. 12b showed that the corroded surface ratio became even higher for the

ECAP samples as compared to the as-received sample, when the current density increased; this was even more marked for the longitudinal section as compared to the transverse section, as previously observed (Fig. 11). Moreover, Fig. 12c showed that, when the current density increased, the pit density increased for all samples, as expected; moreover, the pit densities values were quite similar for all samples for a low current density (100 µA cm^{-2}), but became higher for ECAP samples as compared to the as-received sample when the current density increased. Considering all the results, i.e. both representative 2D/3D profiles (Figs. 10 and 11) and the statistical analysis of the pit morphology (Fig. 12), it could be concluded that ECAP promoted the pit propagation via increased surface area rather than in depth, enhancing also the pit propagation in the forming direction. Furthermore, the increase in corroded surface area for ECAP samples could be explained by considering both an increase in pit width (Figs. 10 and 11) and in pit density (Fig. 12c). Concerning the increase in pit density for ECAP samples, as compared to the as-received sample, this could be related to the fragmentation of the Fe-rich IMCs, as shown by Fig. 5. ECAP led to a multiplication of the pit initiation sites due to the fragmentation of the Fe-rich IMCs. When the current density was increased, more Fe-rich IMCs became pit initiation sites for ECAP samples, which participated in the lateral propagation of the corrosion rather than in-depth propagation. However, it should be noted here that the pit density parameter was rather difficult to estimate due to the pit propagation mechanism itself. Indeed, Fig. 13 shows SEM observations of pits grown on both as-received, ECAP-RR and ECAP-RH samples polarised with a current density of 7 mA cm^{-2} for 10 minutes. All samples exhibited large active pits initiating at Fe-rich IMCs (circle in Fig. 13c), and corrosion filaments were observed all around the pits indicating pit propagation along grain boundaries that intersected the growing pits in the surrounding matrix of IMCs. The large-scale crystallographic dissolution observed in Fig. 13a, b and c was most likely due to the presence of internal crystallographic defects inside the surrounding matrix, which has been observed in other studies

[73–74]. The lateral propagation of pits through the filaments led to the coalescence of different pits as shown in Fig. 13d. Such a phenomenon was likely to induce an artefact in the determination of the pit density (Fig. 12c). Besides, some 3D profiles (Fig. 11f) clearly showed large pits that seemed constituted of several small coalescing pits. Nevertheless, the most important here was that the pit coalescence was a major phenomenon to explain the lateral pit propagation, and the differences observed between transverse and longitudinal sections for one part, and the as-received and ECAP samples for the other parts. Indeed, first, the alignment of Fe-rich IMCs along the forming axis (Fig. 5) led to the coalescence of corrosion pits along the same particular axis, i.e. in the longitudinal direction, which could explain that pits propagated more in that direction (Figs. 10, 11 and 12). Furthermore, results showed that pit coalescence proceeded though fine filaments (Fig. 13), which meant that pit propagation was, at least partially, related to the corrosion propagation at the grain boundaries all around the pits. Therefore, the microstructure, and more precisely the grain size and the nature of the grain boundaries all around the pit initiation sites, i.e. Fe-rich IMCs, was of major importance. Fig. 14 shows that, for all samples, the matrix surrounding IMCs was characterised by a larger amount of small grains as compared to the matrix far from the IMCs, so that long bands of small grains aligned in the forming direction were observed around the Fe-rich IMCs. In most cases, those small grains had lower internal misorientation spread levels between 0 and 2°, indicating that they were most likely recrystallised grains (Fig. 14g to l). Besides, ACOM observations also showed different crystallographic orientations in the vicinity of Fe-rich IMCs when compared to the matrix. These analyses clearly indicated an effect of IMCs on the surrounding matrix microstructure, in agreement with the particle stimulated nucleation (PSN) phenomenon described in literature [53,75–76]. PSN is associated with the formation of a deformation zone around IMCs called the Precipitate Deformation Zone (PDZ), which results from the plastic relaxation of dislocation arrays in the vicinity of IMCs. It generally results in nucleation of grains and texture modification around IMCs when deformation is applied during processing of the material, which is the case during both extrusion and ECAP processes. The new crystallographic orientation observed around IMCs are dependent on the initial orientation of the grains [77–78]. Fig. 14 showed that IMCs generated a quite random texture in their surroundings with either <111>, <100> or <101> directions emerging in the PDZ. Clearly, such microstructural changes could be of major importance for the corrosion behaviour of the material. Indeed, Parvizi et al. showed that localised corrosion was triggered by high-density nano-scale dislocation structures formed in the vicinity of precipitates [76]. The formation of new grains with new textures by PSN created new pathways for localised corrosion. In order to test such an assumption, transmission Kikuchi diffraction images of zones previously identified by SEM were recorded for the as-received sample before and after corrosion tests in order to study the pit propagation from the Fe-rich IMCs. Fig. 15 gives an example of such an analysis for one selected zone. Figure 15a corresponds to the transmission Kikuchi diffraction image of the selected zone, where the black spot corresponds to a Fe-rich IMC as observed by SEM (Fig. 15d). Figs. 15b and c correspond to the analyses performed after a 12-h and a 24-h immersion in 3M NaCl, respectively. Figs. 15e and f are the corresponding SEM observations. It should be noted here that, due to the carbon contamination induced by the SEM observation, a long immersion time in a concentrated electrolyte was necessary to make the pit grow. Figs. 15e and f evidenced the pit propagation from the Fe-rich IMC when the immersion time increased. The corresponding transmission Kikuchi images clearly showed that the pit propagated preferentially in the small grains constituting the PDZ. Such a result highlighted the influence of the deformation on the pit propagation. Further, considering that the ECAP process led to a grain refinement (Figs. 1 and 2) combined with an increase in the HAGB density (Fig. 3), it could be reasonably assumed that, for ECAP samples, pits should propagate from the Fe-rich IMCs, with even more numerous filaments spreading from the pits and linked to the corrosion of all HAGBs, known to be highly reactive. In that sense, the increase in HAGBs amount in the ECAP samples should contribute also to the lateral propagation of the pits [79]. Moreover, the organisation of the small grains in bands aligned in the forming direction (Fig. 14d, j, l), all around the Fe-rich IMCs, promoted the propagation of the pits in this specific direction. Finally, for ECAP samples, the proximity of the different pits, due to Fe-rich IMCs fragmentation, combined with the propensity of the pits to propagate laterally due to the presence of small grains all around the IMCs, promoted pit coalescence, and therefore the increase in width of the pits.

4 Conclusions

The influence of ECAP processes, one with two passes at room temperature (ECAP-RR) and the other with the second pass at 150 °C (ECAP-RH), on the microstructure and the corrosion behaviour of an Al-Mg-Si aluminium alloy used for automotive conductors was investigated. The main conclusions are as follows:

- The grain structure was strongly influenced by both ECAP-RR and ECAP-RH processes, with a grain refinement observed as compared to the as-received sample. The increase in processing temperature during ECAP-RH led to the complete recrystallisation of the microstructure, whereas, in the case of the ECAP-RR sample, only an incomplete recrystallisation process occurred. This resulted in a much more homogeneous grain distribution with less stored deformation for the ECAP-RH sample when compared to the ECAP-RR sample.
- An increase in the mechanical properties after ECAP was demonstrated, the ECAP-RR sample showing the highest R_m values. This was attributed to a decrease in grain size and an increase in the dislocation density during ECAP. The increase in the processing temperature during ECAP-RH led to a softening of the alloy compared to the ECAP-

RR sample most likely due to the complete recrystallisation process related to a low dislocation density.

- The ECAP processing parameters used in this study did not induce the formation of intragranular and intergranular Mg_2Si type precipitates. This was explained considering that the as-received sample, on which ECAP was applied, had a highly deformed microstructure.
- ECAP did not lead to a significant change in the polarisation curves obtained in NaCl solution for the Al-Mg-Si alloy. The corrosion mechanisms were not modified and, for all samples, pitting corrosion was observed.
- However, significant changes in the pitting corrosion behaviour was observed after ECAP. First, an increase in the pit density was observed for ECAP samples as compared to the as-received sample. This was explained by considering the fragmentation of Fe-rich IMCs during the ECAP process, which led to the multiplication of pit initiation sites. The increase in the pit density for ECAP samples could explain the increase in the corroded surface ratio for those samples as compared to the as-received samples, whereas the pit depth decreased. Nevertheless, globally, for ECAP samples, pits were also found to be larger than those observed for the as-received sample, showing that ECAP promoted pit propagation laterally on the surface rather than increasing pit depth. Such a result was explained considering the microstructural changes due to the ECAP process. Results showed that pit propagation proceeded through fine filaments generated by the dissolution of the grain boundaries that intersected the pits. Due to the fact that ECAP induced a global increase in the HAGB density, but with an overconcentration of HAGBs surrounding the Fe-rich IMCs, pits grew laterally more than they deepened. Moreover, lateral expansion of pits combined with closer pit

proximity due to the multiplication of pit initiation sites promoted the formation of coalescing pits.

Acknowledgments

This research has benefited from characterisation equipment of the Grenoble INP - CMTC platform supported by the Centre of Excellence of Multifunctional Architectured Materials (CEMAM) n°ANR-10-LABX-44-01, funded by the Investments for the Future program. The authors thank the ANRT (Association Nationale Recherche Technologie) for the financial support. They also thank Arnaud Proietti (Raimond Castaing Microanalysis Center, Toulouse, France) who performed all the EBSD analyses.

Data availability

The raw/processed data required to reproduce these findings cannot be shared at this time as the data also forms part of an ongoing study.

5 References

[1] S. Koch, H. Antrekowitsch, Aluminum Alloys for Wire Harnesses in Automotive Engineering, BHM Berg- Hüttenmänn. Monatshefte. 152 (2007) 62–67. doi:10.1007/s00501-007-0275-z.

[2] A. Laurino, Intégration des alliages d'aluminium dans le câblage électrique automobile : procédés de mise en forme, microstructure et durabilité, Doctoral dissertation, Université de Toulouse, 2012.

[3] T.G. Langdon, Twenty-five years of ultrafine-grained materials: Achieving exceptional properties through grain refinement, Acta Mater. 61 (2013) 7035–7059. doi:10.1016/j.actamat.2013.08.018.

[4] M. Murashkin, A. Medvedev, V. Kazykhanov, A. Krokhin, G. Raab, N. Enikeev, R.Z. Valiev, Enhanced Mechanical Properties and Electrical Conductivity in Ultrafine-Grained Al 6101 Alloy Processed via ECAP-Conform, Metals. 5 (2015) 2148–2164. doi:10.3390/met5042148.

[5] W.J. Kim, C.S. Chung, D.S. Ma, S.I. Hong, H.K. Kim, Optimization of strength and ductility of 2024 Al by equal channel angular pressing (ECAP) and post-ECAP aging, Scr. Mater. 49 (2003) 333–338. doi:10.1016/S1359-6462(03)00260-4.

[6] M. Hockauf, L.W. Meyer, D. Nickel, G. Alisch, T. Lampke, B. Wielage, L. Krüger, Mechanical properties and corrosion behaviour of ultrafine-grained AA6082 produced by equal-channel angular pressing, J. Mater. Sci. 43 (2008) 7409–7417. doi:10.1007/s10853-008-2724-9.

[7] S. Dadbakhsh, A. Karimi Taheri, C.W. Smith, Strengthening study on 6082 Al alloy after combination of aging treatment and ECAP process, Mater. Sci. Eng. A. 527 (2010) 4758–4766. doi:10.1016/j.msea.2010.04.017.

[8] E.A. El-Danaf, Mechanical properties, microstructure and texture of single pass equal channel angular pressed 1050, 5083, 6082 and 7010 aluminum alloys with different dies, Mater. Des. 32 (2011) 3838–3853. doi:10.1016/j.matdes.2011.03.006.

[9] M.H. Goodarzy, H. Arabi, M.A. Boutorabi, S.H. Seyedein, S.H. Hasani Najafabadi, The effects of room temperature ECAP and subsequent aging on mechanical properties of 2024 Al alloy, J. Alloys Compd. 585 (2014) 753–759. doi:10.1016/j.jallcom.2013.09.202.

[10] Y. Duan, L. Tang, G. Xu, Y. Deng, Z. Yin, Microstructure and mechanical properties of 7005 aluminum alloy processed by room temperature ECAP and subsequent annealing, J. Alloys Compd. 664 (2016) 518–529. doi:10.1016/j.jallcom.2016.01.022.

[11] R.Z. Valiev, T.G. Langdon, Principles of equal-channel angular pressing as a processing tool for grain refinement, Prog. Mater. Sci. 51 (2006) 881–981. doi:10.1016/j.pmatsci.2006.02.003.

[12] A. Korchef, A. Kahoul, Corrosion Behavior of Commercial Aluminum Alloy Processed by Equal Channel Angular Pressing, Int. J. Corros. 2013 (2013) 1–11. doi:10.1155/2013/983261.

[13] D.M. Jafarlou, E. Zalnezhad, M.A. Hassan, M.A. Ezazi, N.A. Mardi, A.M.S. Hamouda, M. Hamdi, G.H. Yoon, Severe plastic deformation of tubular AA 6061 via equal channel angular pressing, Mater. Des. 90 (2016) 1124–1135. doi:10.1016/j.matdes.2015.11.026.

[14] M. Ciemiorek, W. Chrominski, L. Olejnik, M. Lewandowska, Evaluation of mechanical properties and anisotropy of ultra-fine grained 1050 aluminum sheets produced by incremental ECAP, Mater. Des. 130 (2017) 392–402. doi:10.1016/j.matdes.2017.05.069.

[15] T. Khelfa, M.A. Rekik, J.A. Muñoz-Bolaños, J.M. Cabrera-Marrero, M. Khitouni, Microstructure and strengthening mechanisms in an Al-Mg-Si alloy processed by equal channel

angular pressing (ECAP), Int. J. Adv. Manuf. Technol. 95 (2018) 1165-1177. doi:10.1007/s00170-017-1310-1.

[16] O. Sitdikov, E. Avtokratova, T. Sakai, Microstructural and texture changes during equal channel angular pressing of an Al–Mg–Sc alloy, J. Alloys Compd. 648 (2015) 195–204. doi:10.1016/j.jallcom.2015.06.029.

[17] B. Adamczyk-Cieslak, J. Mizera, K.J. Kurzydlowski, Microstructures in the 6060 aluminium alloy after various severe plastic deformation treatments, Mater. Charact. 62 (2011) 327–332. doi:10.1016/j.matchar.2011.01.009.

[18] Y. Zheng, B. Luo, Z. Bai, J. Wang, Y. Yin, Study of the Precipitation Hardening Behaviour and Intergranular Corrosion of Al-Mg-Si Alloys with Differing Si Contents, 7 (2017) 387–399. doi:10.3390/met7100387.

[19] A.K. Bhattamishra, K. Lal, Microstructural studies on the effect of Si and Cr on the intergranular corrosion in Al-Mg-Si alloys, Mater. Des. 18 (1997) 25–28. doi:10.1016/S0261-3069(97)00027-7.

[20] G. Svenningsen, M.H. Larsen, J.C. Walmsley, J.H. Nordlien, K. Nisancioglu, Effect of artificial aging on intergranular corrosion of extruded AlMgSi alloy with small Cu content, Corros. Sci. 48 (2006) 1528–1543. doi:10.1016/j.corsci.2005.05.045.

[21] G. Svenningsen, M.H. Larsen, J.H. Nordlien, K. Nisancioglu, Effect of high temperature heat treatment on intergranular corrosion of AlMgSi(Cu) model alloy, Corros. Sci. 48 (2006) 258–272. doi:10.1016/j.corsci.2004.12.003.

[22] G. Svenningsen, J.E. Lein, A. Bjørgum, J.H. Nordlien, Y. Yu, K. Nisancioglu, Effect of low copper content and heat treatment on intergranular corrosion of model AlMgSi alloys, Corros. Sci. 48 (2006) 226–242. doi:10.1016/j.corsci.2004.11.025.

[23] D. Zander, C. Schnatterer, C. Altenbach, V. Chaineux, Microstructural impact on intergranular corrosion and the mechanical properties of industrial drawn 6056 aluminum wires, Mater. Des. 83 (2015) 49–59. doi:10.1016/j.matdes.2015.05.079.

[24] A. Laurino, E. Andrieu, J.-P. Harouard, J. Lacaze, M.-C. Lafont, G. Odemer, C. Blanc, Corrosion Behavior of 6101 Aluminum Alloy Strands for Automotive Wires, J. Electrochem. Soc. 160 (2013) C569–C575. doi:10.1149/2.080311jes.

[25] J.O. Park, C.H. Paik, Y.H. Huang, R.C. Alkire, Influence of Fe-Rich Intermetallic Inclusions on pit iniation on Aluminium alloy in aerated NaCl, J. Electrochem. Soc. 146 (1999) 517–523. doi:10.1149/1.1391637

[26] D. Song, A. Ma, J. Jiang, P. Lin, D. Yang, Corrosion behavior of ultra-fine grained industrial pure Al fabricated by ECAP, Trans. Nonferrous Met. Soc. China. 19 (2009) 1065–1070. doi:10.1016/S1003-6326(08)60407-0.

[27] K.D. Ralston, N. Birbilis, C.H.J. Davies, Revealing the relationship between grain size and corrosion rate of metals, Scr. Mater. 63 (2010) 1201–1204. doi:10.1016/j.scriptamat.2010.08.035.

[28] M.I. Abd El Aal, M.M. Sadawy, Influence of ECAP as grain refinement technique on microstructure evolution, mechanical properties and corrosion behavior of pure aluminum, Trans. Nonferrous Met. Soc. China. 25 (2015) 3865–3876. doi:10.1016/S1003-6326(15)64034-1.

[29] H. Miyamoto, Corrosion of Ultrafine Grained Materials by Severe Plastic Deformation, an Overview, Mater. Trans. 57 (2016) 559–572. doi:10.2320/matertrans.M2015452.

[30] J.G. Brunner, N. Birbilis, K.D. Ralston, S. Virtanen, Impact of ultrafine-grained microstructure on the corrosion of aluminium alloy AA2024, Corros. Sci. 57 (2012) 209–214. doi:10.1016/j.corsci.2011.12.016.

[31] K.D. Ralston, D. Fabijanic, N. Birbilis, Effect of grain size on corrosion of high purity aluminium, Electrochimica Acta. 56 (2011) 1729–1736. doi:10.1016/j.electacta.2010.09.023.

[32] S.H. Kim, U. Erb, K.T. Aust, Grain boundary Character distribution and intergranular corrosion behavior in high purity aluminium, Scripta Mater. 44 (2001) 835–839. doi:10.1016/S1359-6462(00)00682-5.

[33] C. Xu, S. Schroeder, P.B. Berbon, T.G. Langdon, Principles of ECAP–Conform as a continuous process for achieving grain refinement: Application to an aluminum alloy, Acta Mater. 58 (2010) 1379–1386. doi:10.1016/j.actamat.2009.10.044.

[34] M. Furukawa, Y. Iwahashi, Z. Horita, M. Nemoto, T.G. Langdon, The shearing characteristics associated with equal-channel angular pressing, Mater. Sci. Eng. A. 257 (1998) 328–332. doi:10.1016/S0921-5093(98)00750-3.

[35] B. Beausir, J.-J. Fundenberger, Analysis Tools for Electron and X-ray diffraction, ATEX - software, Université de Lorraine, Metz, n.d. www.atex-software.eu.

[36] E.F. Rauch, M. Véron, Automated crystal orientation and phase mapping in TEM, Mater. Charact. 98 (2014) 1–9. doi:10.1016/j.matchar.2014.08.010.

[37] B. Bay, N. Hansen, D.A. Hughes, D. Kuhlmann-Wilsdorf, Overview no. 96 evolution of f.c.c. deformation structures in polyslip, Acta Metall. Mater. 40 (1992) 205–219. doi:10.1016/0956-7151(92)90296-Q.

[38] Y.H. Zhao, X.Z. Liao, Z. Jin, R.Z. Valiev, Y.T. Zhu, Microstructures and mechanical properties of ultrafine grained 7075 Al alloy processed by ECAP and their evolutions during annealing, Acta Mater. 52 (2004) 4589–4599. doi:10.1016/j.actamat.2004.06.017.

[39] M. Suresh, A. Sharma, A.M. More, R. Kalsar, A. Bisht, N. Nayan, S. Suwas, Effect of equal channel angular pressing (ECAP) on the evolution of texture, microstructure and mechanical properties in the Al-Cu-Li alloy AA2195, J. Alloys Compd. 785 (2019) 972–983. doi:10.1016/j.jallcom.2019.01.161.

[40] P.B. Prangnell, J.S. Hayes, J.R. Bowen, P.J. Apps, P.S. Bate, Continuous recrystallisation of lamellar deformation structures produced by severe deformation, Acta Mater. 52 (2004) 3193–3206. doi:10.1016/j.actamat.2004.03.019.

[41] H. Jazaeri, F.J. Humphreys, The transition from discontinuous to continuous recrystallization in some aluminium alloys: II – annealing behaviour, Acta Mater. 52 (2004) 3251–3262. doi:10.1016/j.actamat.2004.03.031.

[42] S. Suwas, R. Arruffat Massion, L.S. Tóth, J.-J. Fundenberger, B. Beausir, Evolution of texture during equal channel angular extrusion of commercially pure aluminum: Experiments and simulations, Mater. Sci. Eng. A. 520 (2009) 134–146. doi:10.1016/j.msea.2009.05.028.

[43] Z.C. Wang, P.B. Prangnell, Microstructure refinement and mechanical properties of severely deformed Al–Mg–Li alloys, Mater. Sci. Eng. A. 328 (2002) 87–97. doi:10.1016/S0921-5093(01)01681-1.

[44] D.A. Hughes, N. Hansen, High angle boundaries formed by grain subdivision mechanisms, Acta Mater. 45 (1997) 3871–3886. doi:10.1016/S1359-6454(97)00027-X.

[45] M.H. Shaeri, M. Shaeri, M. Ebrahimi, M.T. Salehi, S.H. Seyyedein, Effect of ECAP temperature on microstructure and mechanical properties of Al–Zn–Mg–Cu alloy, Prog. Nat. Sci. Mater. Int. 26 (2016) 182–191. doi:10.1016/j.pnsc.2016.03.003.

[46] Y.Y. Wang, P.L. Sun, P.W. Kao, C.P. Chang, Effect of deformation temperature on the microstructure developed in commercial purity aluminum processed by equal channel angular extrusion, Scr. Mater. 50 (2004) 613–617. doi:10.1016/j.scriptamat.2003.11.027.

[47] A. Goloborodko, O. Sitdikov, R. Kaibyshev, H. Miura, T. Sakai, Effect of pressing temperature on fine-grained structure formation in 7475 aluminum alloy during ECAP, Mater. Sci. Eng. A. 381 (2004) 121–128. doi:10.1016/j.msea.2004.04.049.

[48] I. Mazurina, T. Sakai, H. Miura, O. Sitdikov, R. Kaibyshev, Effect of deformation temperature on microstructure evolution in aluminum alloy 2219 during hot ECAP, Mater. Sci. Eng. A. 486 (2008) 662–671. doi:10.1016/j.msea.2007.09.070.

[49] A. Yamashita, D. Yamaguchi, Z. Horita, T.G. Langdon, Influence of pressing temperature on microstructural development in equal-channel angular pressing, Mater. Sci. Eng. A. 287 (2000) 100–106. doi:10.1016/S0921-5093(00)00836-4.

[50] K. Majchrowicz, Z. Pakieła, W. Chrominski, M. Kulczyk, Enhanced strength and electrical conductivity of ultrafine-grained Al-Mg-Si alloy processed by hydrostatic extrusion, Mater. Charact. 135 (2018) 104–114. doi:10.1016/j.matchar.2017.11.023.

[51] I.L. Dillamore, W.T. Roberts, Preferred Orientation in Wrought and Annealed Metals, Metall. Rev. 10 (1965) 271–380. doi:10.1179/mtlr.1965.10.1.271.

[52] H.-J. Shin, H.-T. Jeong, D.N. Lee, Deformation and annealing textures of silver wire, Mater. Sci. Eng. A. 279 (2000) 244–253. doi:10.1016/S0921-5093(99)00535-3.

[53] F.J. Humphreys, M. Hatherly, Recrystallization and Related Annealing Phenomena, second ed, Elsevier, 2004. doi:10.1016/B978-0-08-044164-1.X5000-2.

[54] O. Engler, V. Randle, Introduction to Texture Analysis: Macrotexture, Microtexture, and Orientation Mapping, Second Edition, CRC Press., 2009.

[55] S.C. Wang, M.J. Starink, N. Gao, C. Xu, T.G. Langdon, Grain structure and texture development during ECAP of two heat-treatable Al-based alloys, Rev. Adv. Mater. Sci. 10 (2005) 249–255.

[56] S.G. Chowdhury, C. Xu, T.G. Langdon, Texture evolution in an aluminum alloy processed by ECAP with concurrent precipitate fragmentation, Mater. Sci. Eng. A. 473 (2008) 219–225. doi:10.1016/j.msea.2007.05.052.

[57] A.P. Zhilyaev, D.L. Swisher, K. Oh-ishi, T.G. Langdon, T.R. McNelley, Microtexture and microstructure evolution during processing of pure aluminum by repetitive ECAP, Mater. Sci. Eng. A. 429 (2006) 137–148. doi:10.1016/j.msea.2006.05.009.

[58] N.A. Belov, D.G. Eskin, A.A. Aksenov, Iron in Aluminum Alloys : impurity and alloying elements, Taylor & Francis Ltd., 2002.

[59] N.A. Belov, D.G. Eskin, A.A. Aksenov, Chapter 2 - Alloys of the Al–Mg–Si–Fe System, in: Multicomponent Phase Diagr., Elsevier, Oxford, 2005: pp. 47–82. doi:10.1016/B978-008044537-3/50002-0.

[60] V. Guillaumin, G. Mankowski, Influence of overaging treatment on localized corrosion of Al 6056, Corrosion. 56 (2000) 12-23. doi:10.5006/1.3280517

[61] C. Xu, R. Zheng, S. Hanada, W. Xiao, C. Ma, Effect of hot extrusion and subsequent T6 treatment on the microstructure evolution and tensile properties of an Al-6Si-2Cu-0.5Mg alloy, Mater. Sci. Eng. A. 710 (2018) 102–110. doi:10.1016/j.msea.2017.10.052.

[62] R.E. Smallman, A.H.W. Ngan, Physical Metallurgy and Advanced Materials - 7th Edition, Butterworth-Heinemann, 2007.

[63] S. Hirosawa, T. Hamaoka, Z. Horita, S. Lee, K. Matsuda, D. Terada, Methods for Designing Concurrently Strengthened Severely Deformed Age-Hardenable Aluminum Alloys by Ultrafine-Grained and Precipitation Hardenings, Metall. Mater. Trans. A. 44 (2013) 3921–3933. doi:10.1007/s11661-013-1730-y.

[64] A.K. Gupta, D.J. Lloyd, S.A. Court, Precipitation hardening in Al–Mg–Si alloys with and without excess Si, Mater. Sci. Eng. A. 316 (2001) 11–17. doi:10.1016/S0921-5093(01)01247-3.

[65] E.O. Hall, The Deformation and Ageing of Mild Steel: III Discussion of Results, Proc. Phys. Soc. Sect. B. 64 (1951) 747–753. doi:10.1088/0370-1301/64/9/303.

[66] A.H. Chokshi, A. Rosen, J. Karch, H. Gleiter, On the validity of the hall-petch relationship in nanocrystalline materials, Scr. Metall. 23 (1989) 1679–1683. doi:10.1016/0036-9748(89)90342-6.

[67] A. Dubyna, A. Mogucheva, R. Kaibyshev, Hall-petch relationship in an Al-Mg-Sc alloy subjected to ECAP, Adv. Mater. Res. 922 (2014) 120–125. doi:10.4028/www.scientific.net/AMR.922.120.

[68] O. Sitdikov, E. Avtokratova, T. Sakai, K. Tsuzaki, R. Kaibyshev, Y. Watanabe, Effect of Processing Temperature on Microstructure Development during ECAP of Al-Mg-Sc Alloy, Mater. Sci. Forum. 584–586 (2008) 481–486. doi:10.4028/www.scientific.net/MSF.584-586.481.

[69] F. Zeng, Z. Wei, J. Li, C. Li, X. Tan, Z. Zhang, Z. Zheng, Corrosion mechanism associated with Mg2Si and Si particles in Al–Mg–Si alloys, Trans. Nonferrous Met. Soc. China. 21 (2011) 2559–2567. doi:10.1016/S1003-6326(11)61092-3.

[70] J. Ming Wang, X. Dan Meng, Y. Ying Bai, G. Feng Ma, Y. Liu, C. Lin He, Effect of Artificial Aging on Intergranular Corrosion of 6063 Al Alloy, Adv. Mater. Res. 842 (2013) 275–278. doi:10.4028/www.scientific.net/AMR.842.275.

[71] F. Eckermann, T. Suter, P.J. Uggowitzer, A. Afseth, P. Schmutz, The influence of MgSi particle reactivity and dissolution processes on corrosion in Al–Mg–Si alloys, Electrochimica Acta. 54 (2008) 844–855. doi:10.1016/j.electacta.2008.05.078.

[72] R. Ly, K.T. Hartwig, H. Castaneda, Effects of strain localization on the corrosion behavior of ultra-fine grained aluminum alloy AA6061, Corros. Sci. 139 (2018) 47–57. doi:10.1016/j.corsci.2018.04.023.

[73] X. Zhang, X. Zhou, T. Hashimoto, B. Liu, Localized corrosion in AA2024-T351 aluminium alloy: Transition from intergranular corrosion to crystallographic pitting, Mater. Charact. 130 (2017) 230–236. doi:10.1016/j.matchar.2017.06.022.

[74] Z. Ahmad, A. Ul-Hamid, A.-A. B.J, The corrosion behavior of scandium alloyed Al 5052 in neutral sodium chloride solution, Corros. Sci. 43 (2001) 1227–1243. doi:10.1016/S0010-938X(00)00147-5.

[75] L.C.L. Ko, Particle Stimulated Nucleation: Deformation Around Particles, Doctoral dissertation, University of Manchester, 2014.

[76] R. Parvizi, A.E. Hughes, M.Y. Tan, R.K.W. Marceau, M. Forsyth, P. Cizek, A.M. Glenn, Probing corrosion initiation at interfacial nanostructures of AA2024-T3, Corros. Sci. 116 (2017) 98–109. doi:10.1016/j.corsci.2016.12.006.

[77] J.F. Humphreys, P.S. Bate, A. Gholinia, I. Brough, Measuring and Modelling the Microstructures of Two-Phase Aluminium Alloys after Deformation, Mater. Sci. Forum. 715–716 (2012) 23–32. doi:10.4028/www.scientific.net/MSF.715-716.23.

[78] F.J. Humphreys, Local lattice rotations at second phase particles in deformed metals, Acta Metall. 27 (1979) 1801–1814. doi:10.1016/0001-6160(79)90071-3.

[79] O. Jilani, N. Njah, P. Ponthiaux, Transition from intergranular to pitting corrosion in fine grained aluminum processed by equal channel angular pressing, Corros. Sci. 87 (2014) 259–264. doi:10.1016/j.corsci.2014.06.031.

Captions of Figures and Tables

Fig. 1: Orientation maps (parallel to the forming axis) of the as-received (a, b), ECAP-RR (d, e) and ECAP-RH (g, h) samples. Figs. a, d and g show the transverse sections and Figs. b, e and h are for longitudinal sections. Figs. c, f and i represent band contrast images with grain boundaries drawn in black for as-received, ECAP-RR and ECAP-RH samples respectively (area weighted grain size is reported below each image)

Fig. 2: Grain size distribution of as-received, ECAP-RR and ECAP-RH samples (a) number fraction and (b) area fraction. Analyses were performed for the transverse sections (TS).

Fig. 3: (a) Relative fraction of HAGBs and LAGBs; (b) total length of all boundaries, HAGBs and LAGBs. Analyses were performed for the as-received, ECAP-RR and ECAP-RH samples for the transverse sections (TS).

Fig. 4: Pole figures of as-received, ECAP-RR and ECAP-RH samples for the transverse and longitudinal sections.

Fig. 5: (a) and (b) SEM observations of the longitudinal section of ECAP-RR and ECAP-RH samples, respectively. The arrows show the extrusion axis. (c) Fraction in surface area covered by IMCs and (d) IMCs size distribution for the as-received, ECAP-RR and ECAP-RH samples.

Fig. 6: TEM observation of (a) an Al-Fe-Si IMC on the surface of an as-received sample (the corresponding diffraction pattern is also reported), (b) the grain structure in ECAP-RH condition and (c) dislocation arrays in an ECAP-RH sample.

Fig. 7: (a) True stress-strain curves and (b) main mechanical parameters extracted from curves shown in (a).

Fig. 8: Polarisation curves (250 mV h^{-1}) of as-received, ECAP-RR and ECAP-RH samples in 0.5 M NaCl for (a) and (b) the transverse section and (c) and (d) the longitudinal section. (a) and (c) correspond to the cathodic domain whereas (b) and (d) are for the anodic domain. For

each curve, OM observations of ECAP-RR sample at the end of the polarisation are given: the arrow in the OM observation of Fig. d indicates the extrusion axis.

Fig. 9: SEM observation of a Fe-rich IMC after 10 min at OCP in 0.5 M NaCl for the as-received condition.

Fig. 10: 2D profiles obtained by confocal microscopy for pits grown after polarisation during 10 min in 0.5 M NaCl at a fixed current density (a) 100 µA cm^{-2}, (b) 1 mA cm^{-2} and (c) 7 mA cm^{-2} for the as-received, ECAP-RR and ECAP-RH samples in both transverse and longitudinal sections. The lateral scale is reported for each graph.

Fig. 11: 3D profiles obtained by confocal microscopy for pits grown after polarisation during 10 min in 0.5 M NaCl at a current density of 7 mA cm^{-2} for the as-received (a, b), ECAP-RR (c, d) and ECAP-RH (e, f) samples. Figs. a, c and e are for the transverse section and Figs. b, d and f show the longitudinal section. Black circles in Fig. f highlight coalescing pits. The lateral scale is reported for each graph.

Fig. 12: (a) Depth, (b) corroded surface ratio and (c) density of corrosion pits formed for the as-received, ECAP-RR and ECAP-RH samples after polarisation during 10 min in 0.5 M NaCl at a fixed current density of 100 µA cm^{-2}, 1 mA cm^{-2} and 7 mA cm^{-2}.

Fig. 13: SEM observations of corrosion pits after polarisation during 10 min at 7 mA cm^{-2} in 0.5 M NaCl for (a) the as-received, (b) ECAP-RR and (c) ECAP-RH samples. High magnification images are also reported in the right-hand corner of each micrograph. Fig. d shows two examples of coalescing pits formed for an ECAP-RH sample after polarisation during 10 min in 0.5 M NaCl at 7 mA cm^{-2}.

Fig. 14: (a), (b), (c), (d), (e) and (f) Orientation maps (parallel to the forming axis) of the as-received, ECAP-RR and ECAP-RH samples. (g), (h), (i), (j), (k) and (l) Local misorientation maps of the as-received, ECAP-RR and ECAP-RH samples. Arrows indicate the extrusion axis.

Fig. 15: Transmission Kikuchi Diffraction observations of the as-received sample in the longitudinal section performed (a) before immersion, (b) after a 12-hour immersion in 3 M NaCl and (c) after a 24-hour immersion in 3 M NaCl. Corresponding secondary electrons images are reported in Figs. (d), (e) and (f), respectively.

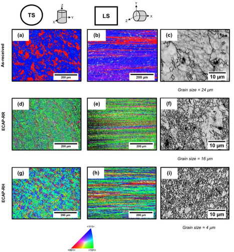

Grain size = 24 µm

Grain size = 16 µm

Grain size = 4 µm

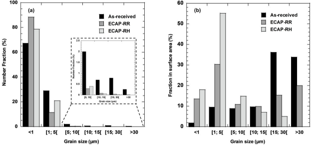
(a)
Number Fraction (%)
0
20
40
60
80
100
As-received
ECAP-RR
ECAP-RH
<1
[1; 5[
[5; 10[
[10; 15[
[15; 30[
>30
Grain size (µm)
Number Fraction (%)
0
0.5
1
1.5
2
2.5
[5; 10[
[10; 15[
[15; 30[
>30
Grain size (µm)
(b)
Fraction in surface area (%)
0
10
20
30
40
50
60
As-received
ECAP-RR
ECAP-RH
<1
[1; 5[
[5; 10[
[10; 15[
[15; 30[
>30
Grain size (µm)


Interface Density (%)
0
20
40
60
80
100
LAGBs
HAGBs
TS
(a)
73.9
52.9
35.4
26.1
47.1
64.6
As-received
ECAP-RR
ECAP-RH
Total boundary length (cm)
0.0
1.0
2.0
3.0
4.0
5.0
All boundaries
LAGBs
HAGBs
(b)
1.58
1.17
0.41
3.67
1.94
1.73
4.24
1.50
2.74
As-received
ECAP-RR
ECAP-RH


TS
Z
Y
X
LS
Y
X
Z
As-received
ECAP-RR
ECAP-RH
{100}
{110}
{111}
Y0
X0
Z0
3
6
9
12
15
2
4
6
8
10
1
2
3
4
1
2
3
4
5
6
2
4
6
8
2
4
6
8

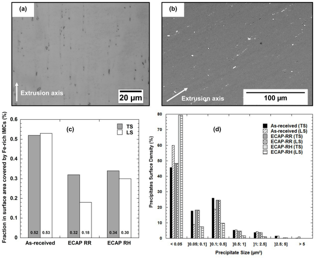
(a)
Extrusion axis
20 µm
(b)
Extrusion axis
100 µm
(c)
Fraction in surface area covered by Fe-rich IMCs (%)
0.6
0.5
0.4
0.3
0.2
0.1
0
TS
LS
0.52
0.53
0.32
0.18
0.34
0.30
As-received
ECAP RR
ECAP RH
(d)
Precipitates Surface Density (%)
80
70
60
50
40
30
20
10
0
As-received (TS)
As-received (LS)
ECAP-RR (TS)
ECAP-RR (LS)
ECAP-RH (TS)
ECAP-RH (LS)
< 0.05
]0.05; 0.1]
]0.1; 0.5]
]0.5; 1]
]1; 2.5]
]2.5; 5]
> 5
Precipitate Size (µm²)

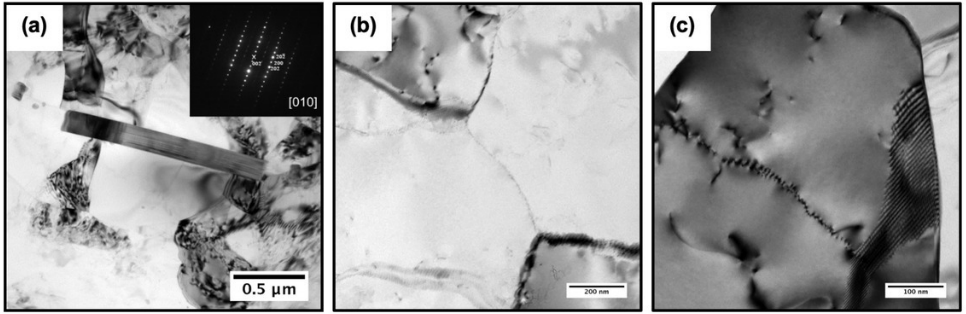
(a)
X
002
20$\bar{2}$
200
202
[010]
0.5 µm
(b)
200 nm
(c)
100 nm

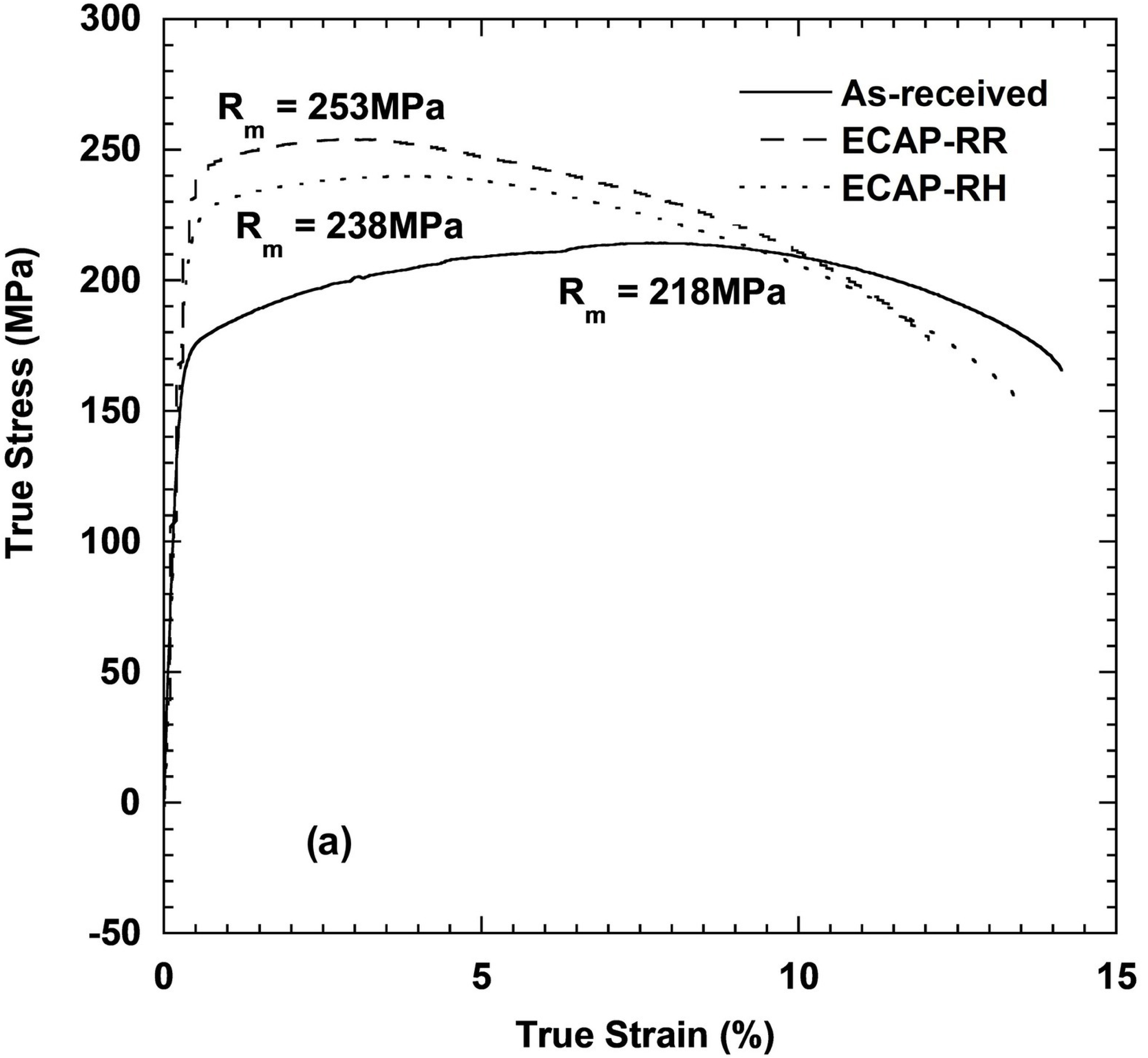

(b)

	As-received	ECAP-RR	ECAP-RH
$R_{p0.2}$ (MPa)	175	243	222
R_m (MPa)	218	253	238
$A_{\%}$ (MPa)	13.9	11.4	13.2

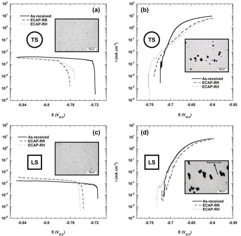
(a)
As-received
ECAP-RR
ECAP-RH
TS
i (mA cm^{-2})
E (V_{SCE})
10^{2}
10^{1}
10^{0}
10^{-1}
10^{-2}
10^{-3}
10^{-4}
10^{-5}
10^{-6}
-0.84
-0.8
-0.76
-0.72
(b)
TS
As-received
ECAP-RR
ECAP-RH
i (mA cm^{-2})
E (V_{SCE})
-0.75
-0.7
-0.65
-0.6
-0.55
(c)
As-received
ECAP-RR
ECAP-RH
LS
i (mA cm^{-2})
E (V_{SCE})
-0.84
-0.8
-0.76
-0.72
(d)
LS
Extrusion axis
As-received
ECAP-RR
ECAP-RH
i (mA cm^{-2})
E (V_{SCE})
-0.75
-0.7
-0.65
-0.6
-0.55

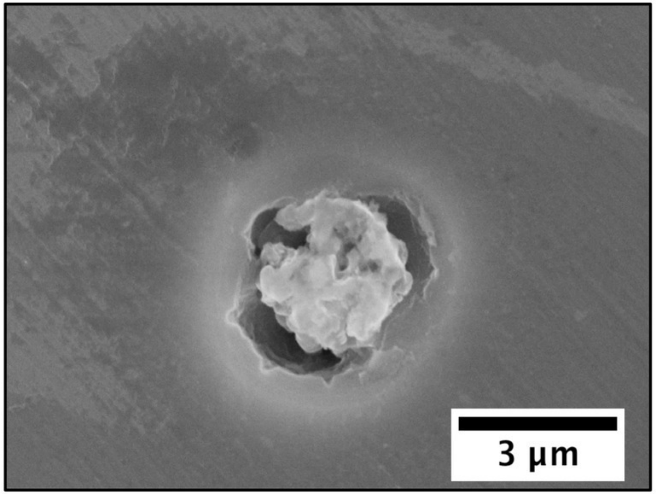
3 µm

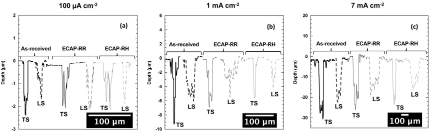
100 µA cm-2
(a)
Depth (µm)
2
1
0
-1
-2
-3
As-received
ECAP-RR
ECAP-RH
TS
LS
TS
LS
TS
LS
100 µm
1 mA cm-2
(b)
Depth (µm)
6
4
2
0
-2
-4
-6
-8
-10
As-received
ECAP-RR
ECAP-RH
TS
LS
TS
LS
LS
100 µm
7 mA cm-2
(c)
Depth (µm)
20
10
0
-10
-20
-30
As-received
ECAP-RR
ECAP-RH
TS
LS
TS
LS
TS
LS
100 µm

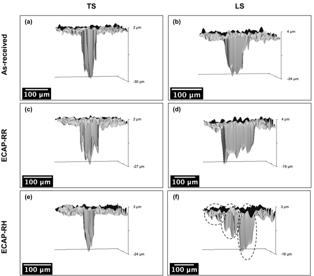
TS
LS
As-received
ECAP-RR
ECAP-RH
(a)
2 µm
-30 µm
100 µm
(b)
4 µm
-24 µm
100 µm
(c)
2 µm
-27 µm
100 µm
(d)
4 µm
-19 µm
100 µm
(e)
3 µm
-24 µm
100 µm
(f)
3 µm
-16 µm
100 µm

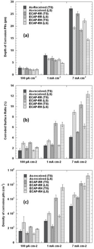
30
25
20
15
10
5
0
Depth of Corrosion Pits (µm)
As-Received (TS)
As-received (LS)
ECAP-RR (TS)
ECAP-RR (LS)
ECAP-RH (TS)
ECAP-RH (LS)
(a)
100 µA cm^{-2}
1 mA cm^{-2}
7 mA cm^{-2}
14
12
10
8
6
4
2
0
Corroded Surface Ratio (%)
As-received (TS)
As-received (LS)
ECAP-RR (TS)
ECAP-RR (LS)
ECAP-RH (TS)
ECAP-RH (LS)
(b)
100 µA cm-2
1 mA cm-2
7 mA cm-2
1 10^4
8 10^3
6 10^3
4 10^3
2 10^3
0
Density of corrosion pits (cm^{-2})
As-received (TS)
As-received (LS)
ECAP-RR (TS)
ECAP-RR (LS)
ECAP-RH (TS)
ECAP-RH (LS)
(c)
100 µA cm-2
1 mA cm-2
7 mA cm-2

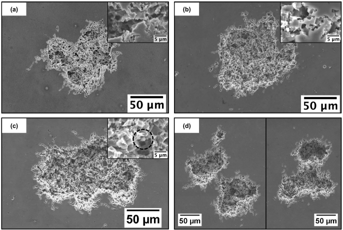
(a)
5 µm
50 µm
(b)
5 µm
50 µm
(c)
5 µm
50 µm
(d)
50 µm
50 µm

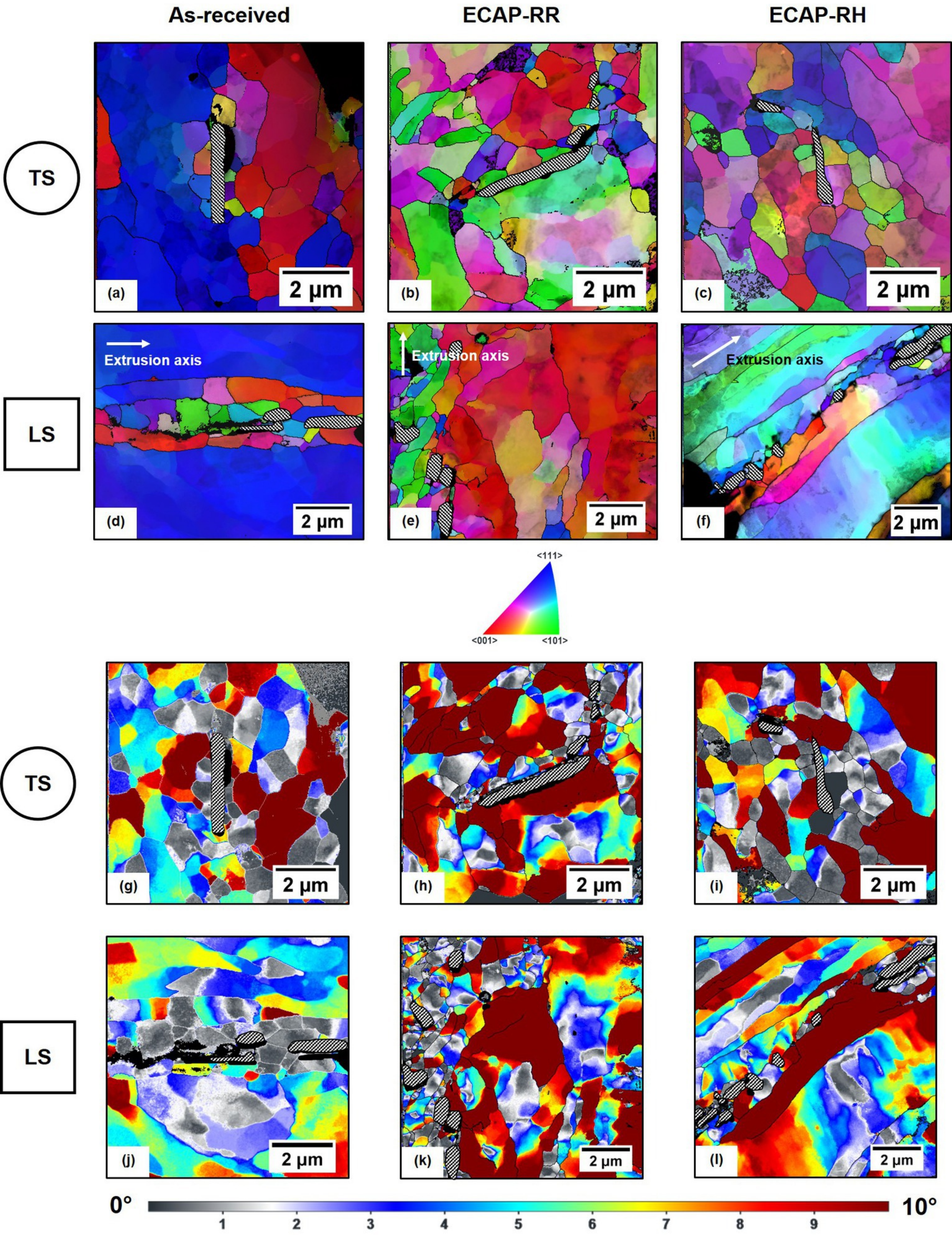
As-received
ECAP-RR
ECAP-RH
TS
LS
(a)
(b)
(c)
(d)
(e)
(f)
(g)
(h)
(i)
(j)
(k)
(l)
2 µm
Extrusion axis
<111>
<001>
<101>
0°
10°
1
2
3
4
5
6
7
8
9

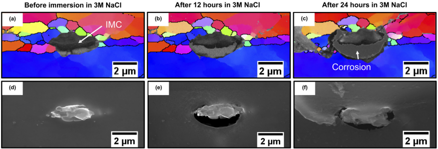
Before immersion in 3M NaCl

After 12 hours in 3M NaCl

After 24 hours in 3M NaCl

As-received (AA6xxx)

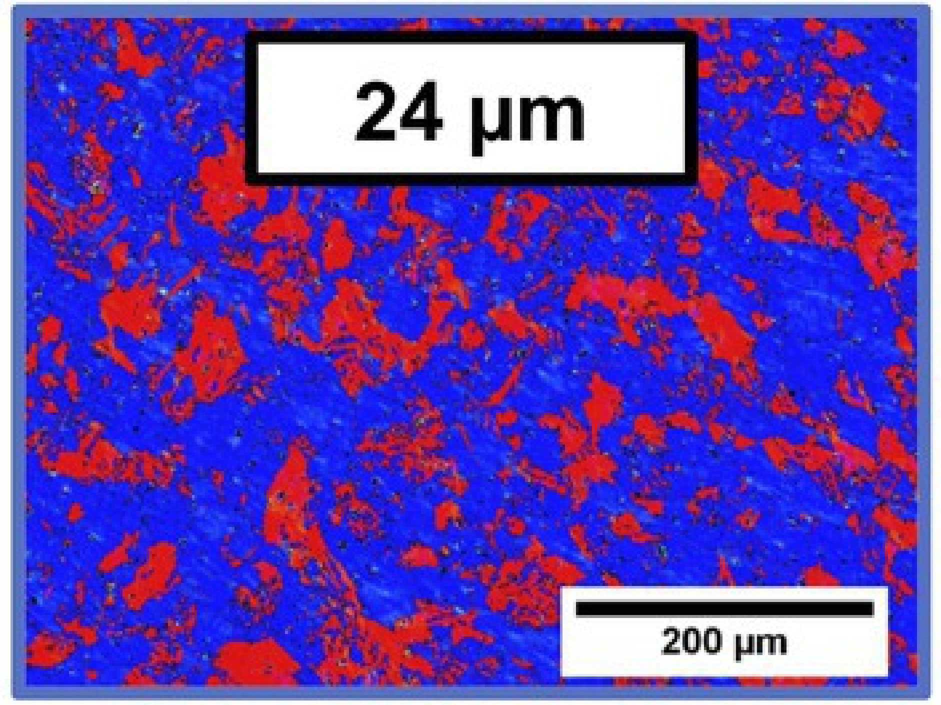

Influence of ECAP on the microstructure

ECAP-RR (25 °C)

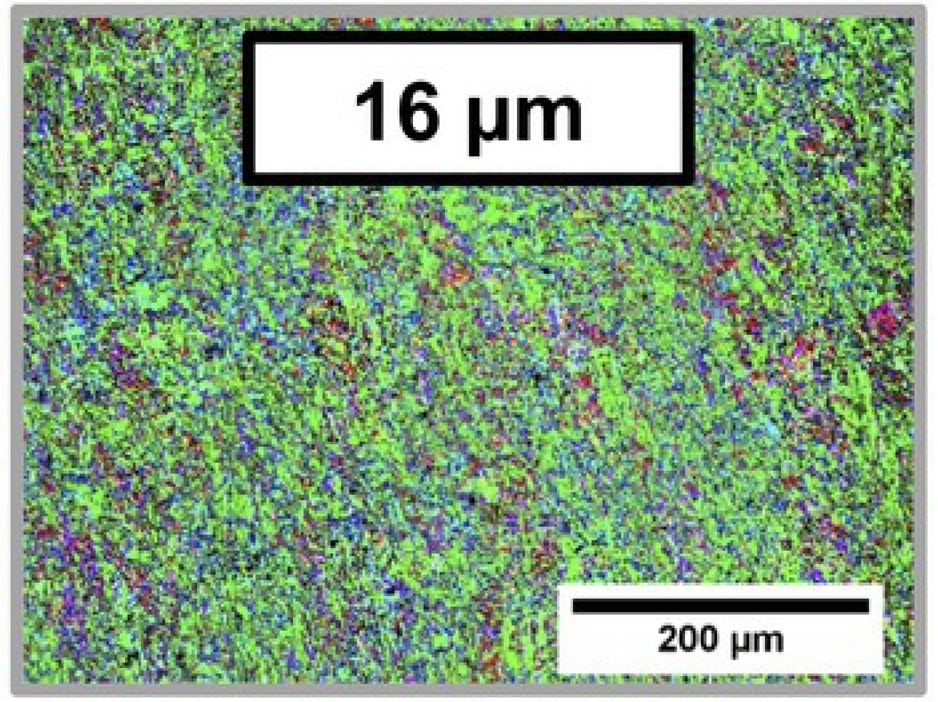

ECAP-RH (150 °C)

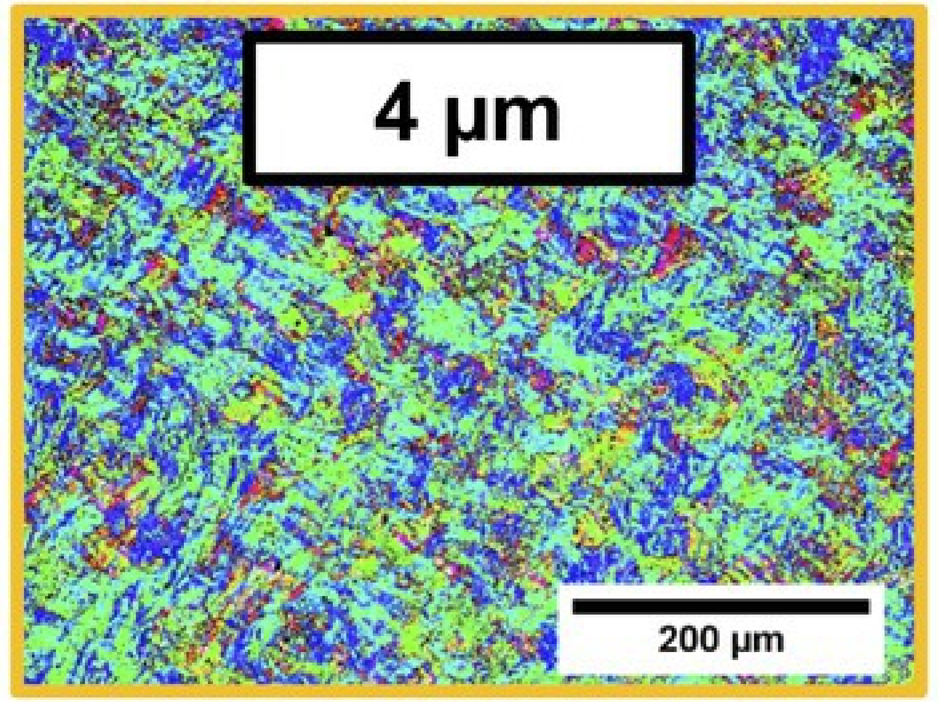

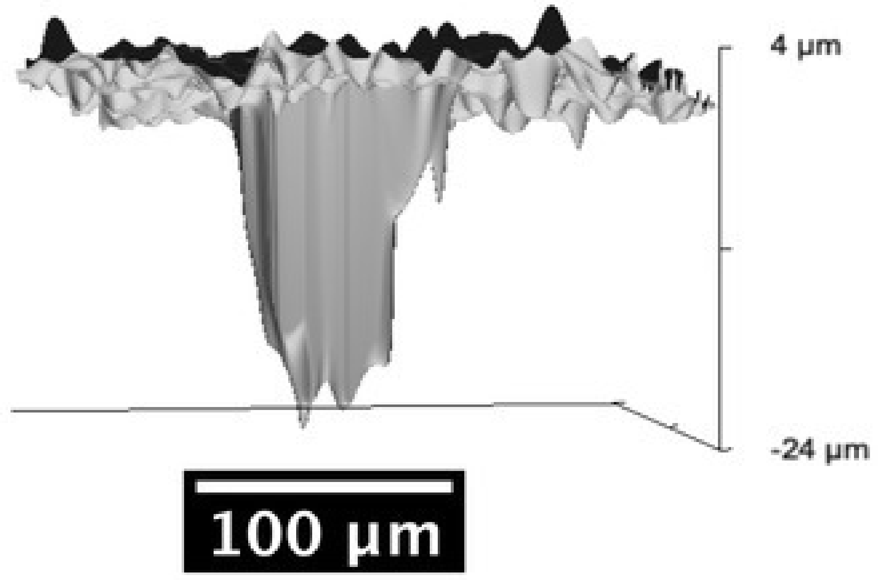

Influence of ECAP on the propagation of corrosion pits

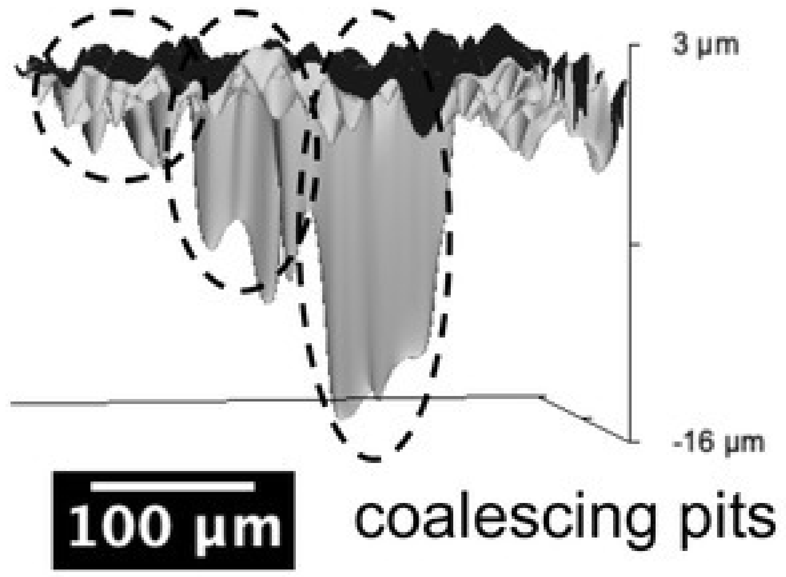

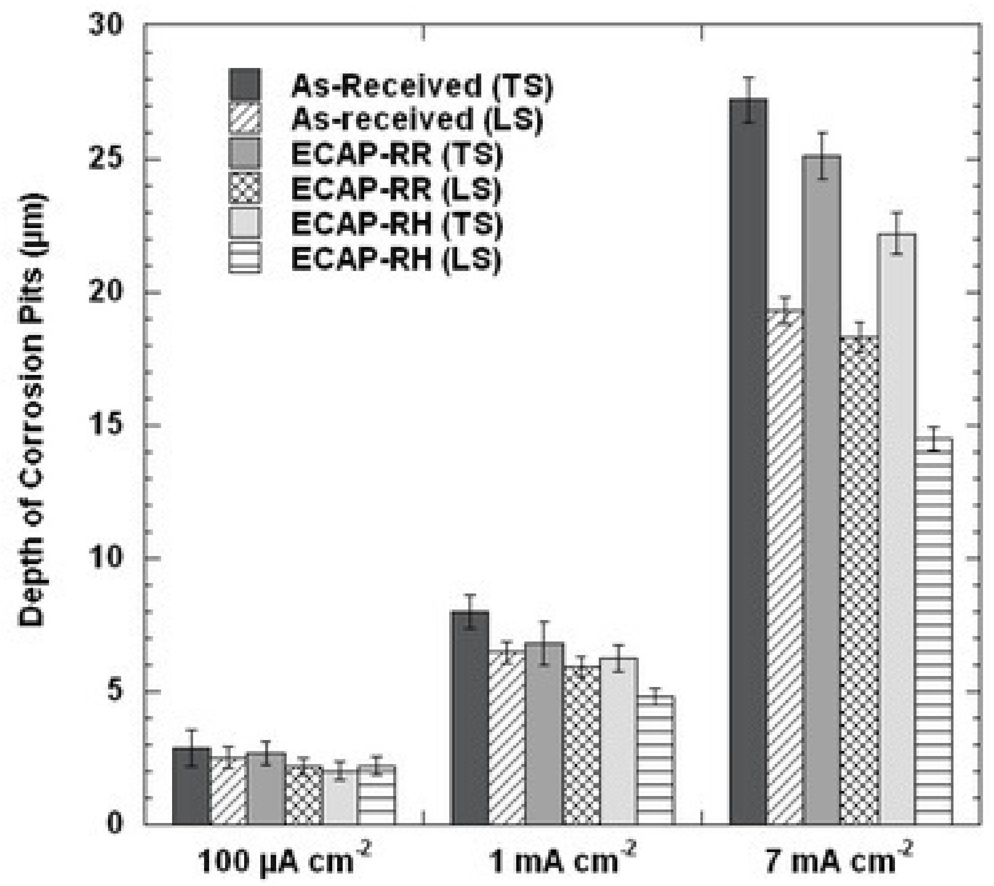

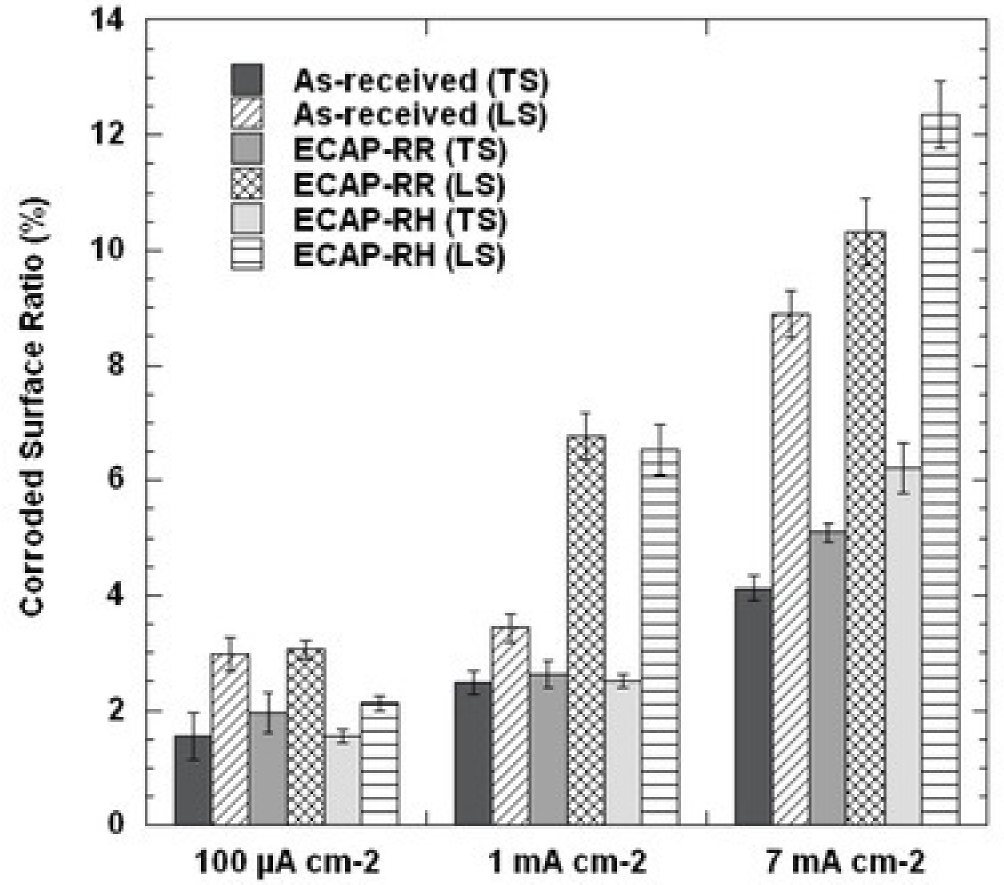

Pits propagate laterally more than in-depth after ECAP